

# Machine learned reconstruction of tsunami dynamics from sparse observations

Edward McDugald<sup>1,2</sup>, Arvind Mohan<sup>2</sup>, Darren Engwirda<sup>3</sup>, Agnese Marcato<sup>4</sup>,  
Javier Santos<sup>4</sup>

<sup>1</sup>University of Arizona

<sup>2</sup>Computer, Computational, and Statistical Sciences Division, Los Alamos National Laboratory

<sup>3</sup>Theoretical Division, Los Alamos National Laboratory

<sup>4</sup>Earth and Environmental Sciences, Los Alamos National Laboratory

## Key Points:

- A transformer model designed for sparse sensing applications known as the Senseiver is modified to reconstruct tsunami waves from sparse measurements corresponding to real sensor locations.
- The model is trained on synthetic surface height fields generated via a shallow water equations numerical simulation, which is shown to provide accurate estimates of historical events.
- The training dataset consists of eight tsunami simulations whose epicenters are sampled from USGS earthquake records along the coast of Japan.
- The extrapolatory capabilities of the Senseiver are probed through inference on tsunami wave data with epicenters not included in training. We also test the physical consistency of the model by adding a soft constraint based on the SWE continuity equation in training.
- The Senseiver yields high accuracy reconstructions for tsunami waves provided that enough information has propagated to the sensors. We discuss how the architecture can be modified to probe optimal sensor placement and process additional information sources referenced in the data assimilation literature.

## Abstract

We investigate the use of the Senseiver, a transformer neural network designed for sparse sensing applications, to estimate full-field surface height measurements of tsunami waves from sparse observations. The model is trained on a large ensemble of simulated data generated via a shallow water equations solver, which we show to be a faithful reproduction for the underlying dynamics by comparison to historical events. We train the model on a dataset consisting of 8 tsunami simulations whose epicenters correspond to historical USGS earthquake records, and where the model inputs are restricted to measurements obtained at actively deployed buoy locations. We test the Senseiver on a dataset consisting of 8 simulations not included in training, demonstrating its capability for extrapolation. The results show remarkable resolution of fine scale phase and amplitude features from the true field, provided that at least a few of the sensors have obtained a non-zero signal. Throughout, we discuss which forecasting techniques can be improved by this method, and suggest ways in which the flexibility of the architecture can be leveraged to incorporate arbitrary remote sensing data (eg. HF Radar and satellite measurements) as well as investigate optimal sensor placements.

## Plain Language Summary

Accurate forecasting of tsunami waves is critical to a functioning early warning system. While physical models of tsunami waves are well-understood and solvable on a computer, the integration of such models at high resolution is computationally expensive and time consuming. The primary source of practical wave-height data is supplied by the DART (Deep-ocean Assessment and Reporting of Tsunami) Network, a series of buoys that provide wave-height measurements throughout the ocean. The challenge we address in this work is in accurately estimating how the ocean free surface evolves in space and time using only the sparse measurements obtained from the DART network. Our experiments are confined to four-hour tsunami simulations with epicenters concentrated near the coast of Japan. Within this limited regime, the number of available non-zero sensors ranges from 0 to 13. We implement and train a transformer-based neural network to reconstruct highly detailed tsunami waves from these incredibly sparse measurements.

## 1 Introduction

Tsunamis are a devastating natural hazard, causing more than 250,000 deaths globally between 1998 and 2017, and US\$280 billion in damages (Imamura et al., 2019). Each year, about 60,000 people and US\$4billion in assets are exposed to tsunami hazard (Bernard & Titov, 2015). Thus, improvements to early warning and forecast systems are highly sought and researched. The majority of existing systems employ PDE-based solvers, in which an initial ocean surface displacement is derived based on estimates of the underlying earthquake dynamics, and a shallow water type PDE model is integrated to predict the propagation of wave fronts over the ocean basin. Such approaches provide so-called ‘full-field’ information to forecasters, including estimates of arrival time, as well as wave amplitude and shape. Various PDE-based models are currently employed both operationally and throughout the research communities, including NOAA’s MOST system (Titov & Gonzalez, 1997), the GeoCLAW solver (Berger et al., 2011; LeVeque et al., 2011), and the Gerris/Basilisk frameworks (Popinet, 2012, 2020). While such systems have produced accurate predictions for a range of historical events, integrating these models is an expensive computational task, requiring massively parallel implementations and resources due to the time-sensitive nature of the problem. The success of such systems is also tied to limitations of the associated PDE model as well as the resolution of the numerical scheme used to solve it.

Due to difficulties in estimating the source and properties of seismic waves, a large class of forecasting methods seek to estimate the wave height field directly. In (Maeda

et al., 2015), a data assimilation method is proposed that combines bottom-pressure gauges and a 2D linear long wave equation to derive wave height and velocity estimates for forecasting. In (Wang, 2022), this method is made more efficient with the use of pre-computed Green's functions. However, this method relies on a dense observation network to be effective. To address this need for dense observations, (Wang et al., 2019) proposed an algorithm based on the Huygens-Fresnel principal to generate virtual observation points from a sparse set of real observation points. In (Fujita et al., 2024), a sensor placement optimization procedure is combined with proper orthogonal decomposition (POD) to perform psuedo-super-resolution, yielding an artificially dense observation network. The latter approach suffers from the reliance on a yet-to-be implemented sensor configuration, and the former suffers from overly simplistic interpolation and limitations on the density of samples. While this work is largely motivated by testing the Senseiver architecture on a variety of highly non-linear realistic phenomena, we note the above works to emphasize the importance of obtaining dense samples for existing data assimilation methods. Thus, the method presented in this work has immediate application to existing forecasting methods.

We propose an attention-based machine learning approach to generate an arbitrarily dense sample of observations from sparse measurements deriving from Deep-ocean Assessment and Reporting of Tsunami Network (DART) buoys. To the best of our knowledge, the only other use of attention mechanisms in the application of sparse sensing of sea surface elevation is in (Archambault et al., 2024), where gap-ridden sea surface height (SSH) measurements are coupled with densely sampled sea surface temperature (SST) data to train an encoder-decoder model that generates densely sampled sea surface height reconstructions. While this approach bears many similarities to the present work in its choice of architecture and application, the problem setup differs significantly in having sea surface elevation fields supported on lines, as well as using full resolution sea temperature fields. While the driving context of this work is in data assimilation based forecasting methods that rely on dense wave height observations, we mention a few notable uses of machine learning in tsunami forecasting. In (Liu et al., 2021), machine learning techniques are used to forecast time series of tsunami wave heights at two fixed gauges in the Puget Sound. Their forecasts are derived from wave height measurements at a hypothetical observation gauge in the Strait of Juan de Fuca. They are able to generate several hours of forecasts at the forecast gauges, given 30-60 minutes of time series data at the observation gauge. In (Rim et al., 2022), CNNs are trained to forecast wave heights at the same forecast gauges from Global Navigation Satellite System data. They demonstrate 6 hours of wave height forecasts given as little as 9 minutes of GNSS data. Notably, this approach allows for the nearly instant use of input data, as there is no lag period to wait for the wave front to interact with a sensor. The use of non-pressure/wave-height measurements such as HF Radar (Wang, Imai, Miyashita, et al., 2023) and distributed acoustic sensing (Xiao et al., 2024) is another exciting realm of forecasting.

We develop a model based on the Senseiver architecture (Santos et al., 2023), a recently developed transformer neural network designed to solve sparse sensing problems. Rather than obtaining full-field predictions using a partial differential equation (PDE) based model, the Senseiver reconstructs such information from a set of observations distributed in space and time. To simulate the realistic application of this system to tsunami forecasting, we adopt NOAA's DART network as sensors — a set of buoys providing high-frequency observations of ocean surface height. While the Senseiver requires only sparse inputs in order to forecast once trained, a dense set of observations are required to learn the behaviour of the system. We use a PDE-based model to generate synthetic tsunamis for given earthquake epicenters, which we sample from historical earthquake records. We assess the skill of the model in reconstructing tsunami waves for unseen events, conducting a series of experiments that assess the quality of the ocean surface height reconstructions at DART buoy locations. We also explore the effect of physics-based regularisation by adding a soft constraint during training that penalises reconstructions violating

physical invariants. In the above referenced forecasting and dense sampling works, the methods are validated by comparing time series of the waveforms at fixed sensor locations. Thus, we include such time series in our assessments. We conclude by outlining future opportunities for the development of Senseiver-based forecasting systems.

## 2 The Senseiver

The tsunami forecast problem can be posed as a sparse sensing challenge: given a discrete set of observations of the ocean state  $s = \{s_1, s_2, \dots, s_N\}$  at locations  $\mathbf{x}^s = \{\mathbf{x}_1^s, \mathbf{x}_2^s, \dots, \mathbf{x}_N^s\}$  and time  $t$ , reconstruct a set of state outputs  $\hat{s} = \{\hat{s}_1, \hat{s}_2, \dots, \hat{s}_M\}$  at a set of query points  $\mathbf{x}^q = \{\mathbf{x}_1^q, \mathbf{x}_2^q, \dots, \mathbf{x}_M^q\}$  and query times  $t^q \geq t$  such that  $M \gg N$ . In this work, the input state  $s(\mathbf{x}^s, t)$  is taken to be the ocean surface height measured at DART buoy locations, and the query state  $\hat{s}(\mathbf{x}^q, t^q)$  is the ocean surface height throughout the remainder of the global ocean domain and at future times  $t^q$ . Noting that DART buoys number only a few dozen, and that even relatively coarse coverage of the global ocean requires at least several hundred thousand discrete points, the reconstruction problem is seen to be extremely sparse.

Recently, the Senseiver (Santos et al., 2023), an attention-based transformer neural network, has been developed to solve such problems — employing a multi-level encoder-decoder architecture to reconstruct dense output from sparse observations. In brief, the model operates as follows:

1. A positional encoder  $P_E$  is used to map the location of observations to a spatial encoding vector  $\mathbf{a}^s$ , with  $s \in \mathbb{R}^N$ .
2. An attention-based encoder  $E$  is used to map the encoded observation/location pairs  $(s_i, \mathbf{a}_i^s)$  to a latent matrix  $\mathbf{Z}$ .
3. The positional encoder  $P_E$  is used to map query locations to a spatial encoding vector  $\mathbf{a}^q$ , with  $q \in \mathbb{R}^M, M \gg N$ .
4. An attention-based decoder  $D$  is used to reconstruct outputs at the encoded query locations  $\mathbf{a}^q$ .

The positional encoder  $P_E$  implements a trigonometric encoding of the spatial coordinates, and the encoder and decoder operators  $E, D$  contain trainable layers in the form of multi-layer perceptrons within their attention blocks. The reader is referred to (Santos et al., 2023) for in-depth discussions of the Senseiver architecture, summarised here as follows

$$\mathbf{a}^s = P_E(\mathbf{x}^s), \quad (1)$$

$$\mathbf{Z} = E(s, \mathbf{a}^s), \quad (2)$$

$$\mathbf{a}^q = P_E(\mathbf{x}^q), \quad (3)$$

$$\hat{s}(\mathbf{x}^q, t^q) = D(\mathbf{Z}, \mathbf{a}^q). \quad (4)$$

While the Senseiver is capable of reconstructing dense output from sparse observations, it must first learn the behaviour of the system through a training procedure in which the weights of the model are optimised by minimising an error measure, here taken to be the mean-squared error

$$\mathcal{L} = \sum \left( s(\mathbf{x}^q, t^q) - \hat{s}(\mathbf{x}^q, t^q) \right)^2, \quad (5)$$

$$\text{where } \hat{s}(\mathbf{x}^q, t^q) = D(E(s(\mathbf{x}^q, t^q), P_E(\mathbf{x}^s)), P_E(\mathbf{x}^q)). \quad (6)$$

Noting that the loss (5) is a summation over the query points  $\mathbf{x}^q$ , here taken to be a dense set covering the global ocean domain, training the model requires that a dense set of state estimates  $s(\mathbf{x}^q, t^q)$  be available, provided in this work by a PDE simulation.

While previous experiments of the Senseiver used data residing on a structured grid, the flexibility of the architecture allows one to seamlessly build a model on unstructured data. Further, the choice of coordinates for the positional encodings are not restricted to the underlying spatial coordinates. For this problem, we added encodings for the ocean bathymetry in addition to latitude and longitude. We also mask out land pixels, training only on data corresponding to ocean pixels. A schematic for the Senseiver workflow is provided in Figure 1.

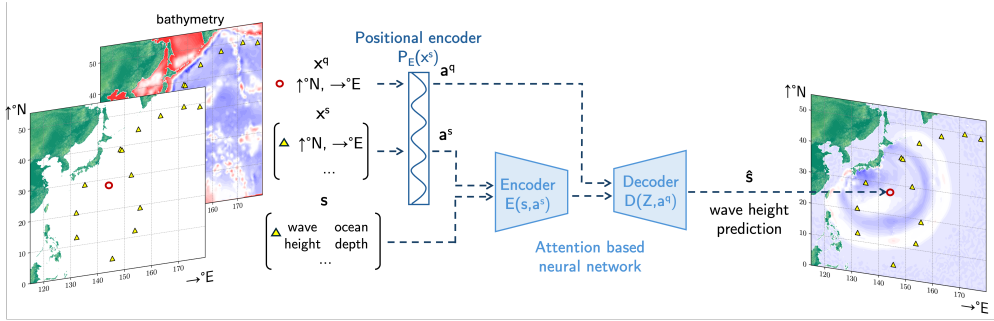


Figure 1: High-level overview of senseiver architecture for tsunami reconstruction

### 3 PDE-based surrogate

Tsunamis can be modelled using the shallow water equations, in which the dynamics of a layer of fluid is represented by a coupled system of PDEs that govern the evolution of the depth-averaged horizontal velocity  $u = u(\mathbf{x}, t)$  and the fluid thickness  $h = h(\mathbf{x}, t)$

$$\frac{\partial u}{\partial t} + (u \cdot \nabla) u + f u^\perp = -(1 - \beta) g \nabla(h + z_b) + c_d \frac{|u|}{h} u + \nu_k^u \nabla^k u, \quad (7)$$

$$\frac{\partial h}{\partial t} + \nabla \cdot (u h) = 0. \quad (8)$$

Here,  $z_b = z(\mathbf{x})$  is the height of the bathymetry at the base of the fluid domain,  $g = 9.80665 \text{ m s}^{-2}$  is the acceleration due to gravity, and  $f = 2\Omega \sin \phi$  is the Coriolis parameter, with  $\Omega = 7.292 \times 10^{-5} \text{ rad s}^{-1}$  being the rotation rate of the Earth and  $\phi$  the angle of latitude.  $u^\perp = \mathbf{k} \times u$ , where  $\mathbf{k}$  is the local vertical direction, is a tangential velocity field used to express the acceleration due to the Coriolis tendency.  $\beta = 0.015$  is a reduced gravity correction that approximates the self-attraction and loading effects associated with tsunami waves (Inazu & Saito, 2013).

The shallow water system can be used to represent the barotropic behaviour of the ocean, in which deformations in the ocean sea surface propagate as gravity waves; mediated by nonlinear advection and rotational effects. The energy loss at the ocean bottom boundary is captured in our model using a logarithmic drag formulation, and grid-scale numerical noise is controlled using an artificial dissipation operator. These sub-grid models are configured with the following drag and viscous scalings

$$c_d = \kappa^2 \log^{-2} \left( 1 + \frac{h}{2z_0} \right), \quad \nu_4^u = \left( \frac{\delta}{\Delta} \right)^3 \bar{\nu}_4^u, \quad (9)$$

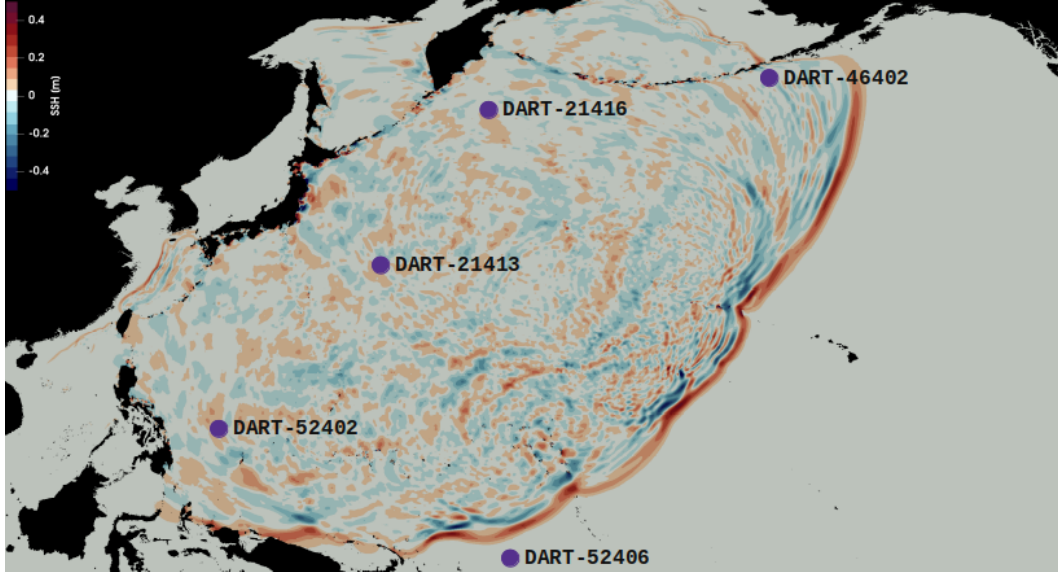


Figure 2: Sea surface height snapshot 6 hours after the Tohoku earthquake event simulated using the PDE-based barotropic model. DART sensor locations used in the analysis are highlighted.

where the bottom roughness  $z_0 = 0.001$  m, the von Karman constant  $\kappa = 0.4$ , and the sub-grid dissipation is modelled using a bi-harmonic operator  $\nabla^{k=4}$  with  $\bar{\nu}_4^u = -1.25 \times 10^{11} \text{ m}^4 \text{ s}^{-1}$ , where  $\delta = \delta(\mathbf{x})$  is the local length-scale of the computational mesh, and a reference length of  $\Delta = 30 \times 10^3$  m is used to control global scaling with resolution.

The system (7–8) is discretised using a staggered, quasi 2nd-order accurate finite-volume/difference scheme (Ringler et al., 2010; Thuburn et al., 2009) based on unstructured Voronoi-type polygonal meshes (Engwirda, 2017). The full global ocean domain is modelled in this study, accounting for spherical geometrical effects. A 3-stage explicit Runge-Kutta method optimised for gravity-wave dynamics (Lilly, Engwirda, et al., 2023) is used to advance the model in time.

A related computational approach recently implemented in the Model for Prediction Across Scales (MPAS-O) has been used to simulate various ocean free surface processes, including global tides (Barton et al., 2022; Pal et al., 2023) as well as hurricane driven storm-surge (Lilly, Capodaglio, et al., 2023). Previously, similar finite-volume type shallow water approaches have been employed in the GeoCLAW (LeVeque et al., 2011; Berger et al., 2011) and the Gerris/Basilisk (Popinet, 2012, 2020) frameworks to simulate tsunami dynamics using quadtree-based adaptive mesh refinement.

### 3.1 Validation: Tohoku tsunami

To establish the utility of our PDE model as a surrogate for real tsunami events we used the 2011 Tohoku event as a verification exercise; comparing the sea surface height time-series simulated by our shallow water model with historical observational data collected by NOAA’s DART buoys (NOAA, 2011).

The model was initialised with a sea surface height consistent with the  $M = 9.0$  event that struck near the axis of the Japan trench at  $38.1035^\circ\text{N}$ ,  $142.861^\circ\text{E}$ . We used a free surface profile based on the waveform inversion of (Fujii et al., 2011) and neglected

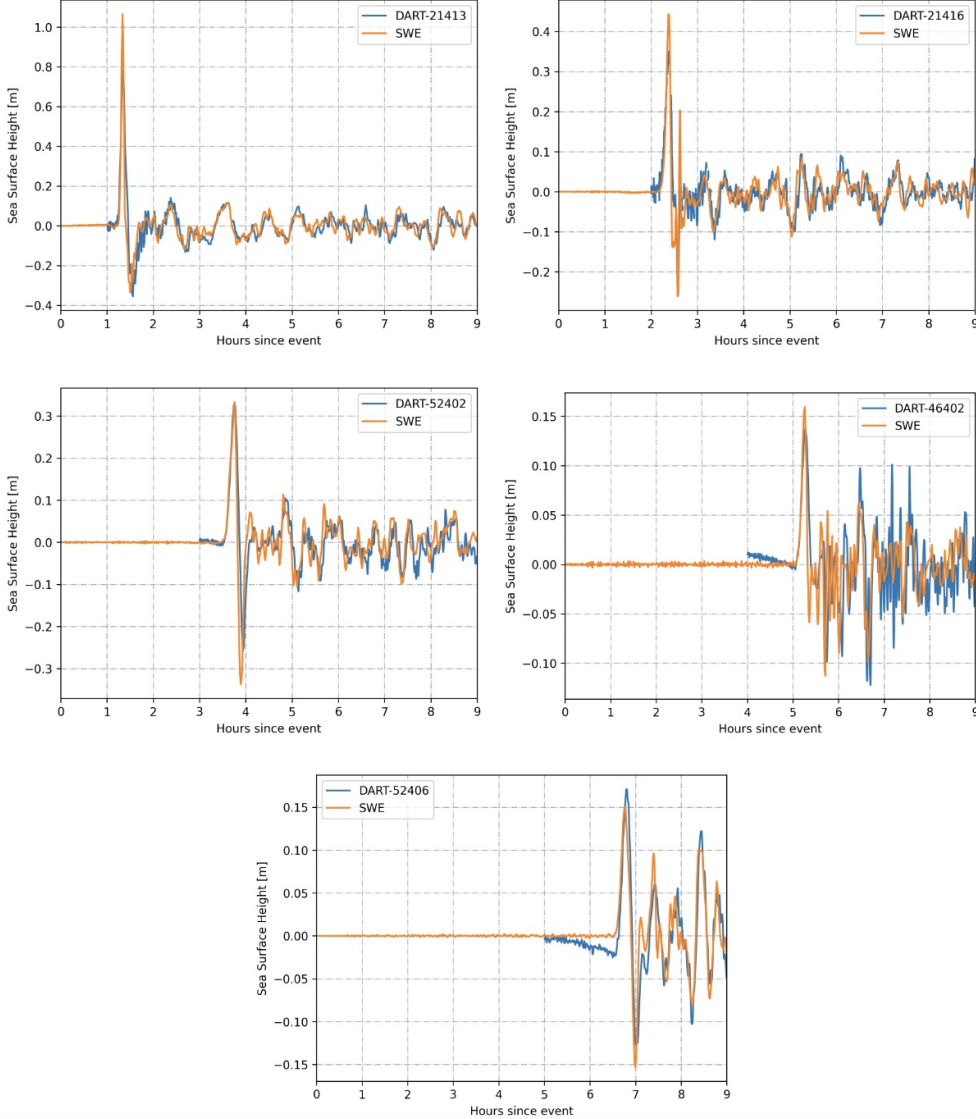


Figure 3: Sea surface height time series at DART sensor locations, comparing DART observations measured following the Tohoku event and output from PDE-based simulations.

initial transients due to coupled ocean-crust interaction. The model was integrated over a period of 12 hours using a time-step of 10 seconds. A variable resolution unstructured mesh was employed, with resolution concentrated in the Northern Pacific region, where a minimum resolution of 1km was placed near coastlines, in shallow regions, and areas of sharp bathymetric gradient, transitioning to a background resolution of 10km throughout the Pacific basin. Globally, coarse 100km mesh resolution was selected to minimise computational overhead. Model bathymetry was interpolated from the GEBCO dataset (GEBCO Compilation Group, 2023) using a consistent remapping procedure. The model was run using 28 cores of an AMD EPYC Milan node hosted via Google's Compute Engine, taking approximately 90 minutes to complete a 12 hour simulation.

A snapshot of simulated sea surface height at  $t = 6$ hrs is shown in Figure 2, illustrating a well resolved wavefront propagating eastward across the Northern Pacific, with complex secondary reflected and refracted waves in the wake. Detailed intercom-

parisons are presented for several DART buoy locations in Figure 3, showing a close match between the simulated and observed data collected by the DART system during the real Tohoku event. Data is sampled from the shallow water solver at 60 second intervals and linearly interpolated from the unstructured model grid to buoy locations. Tides and mean offsets are removed from the DART time series. These results confirm the shallow water model provides a faithful representation of both the amplitude and phase of the propagating waveforms, including an accurate recovery of both the primary pulse as well as the tertiary signals that follow. The close alignment establishes the validity of our shallow water solver as a surrogate for real tsunami events, providing a framework to synthesise sufficiently dense spatio-temporal datasets on which the Senseiver is trained.

## 4 Summary of Model Training and Experiments

### 4.1 Model Training

We trained a total of five models, each composed of eight epicenters. For the mesh used in the SWE solver, each frame is output as an unstructured list of 163,842 tuples, consisting of a longitude/latitude coordinate and a wave height. We subsample each frame by a factor of 2, yielding frames consisting of 81,921 pixels. For each training epicenter, the simulation is run for 144 time steps, with a time step of 50s, effectively giving 2 hour simulations. For all models we used a 95/5 test/train split. The epicenter coordinates used in training were randomly selected from a list of seismic events restricted to the coast of Japan. The models are distinguished by two main attributes: (1) time regime and (2) physical regularization. Since we consider the time regimes of 0-2 hours and 2-4 hours, and both regularized and unregularized training procedures, four models are distinguished. The fifth model concerns the 0-2 hour time regime, and is distinguished by the addition of three artificially placed sensors. This model serves as the basis of a proof-of-concept for future Senseiver experiments to explore optimal sensor placement to improve reconstructions with particularly limited sensor information. The weights of the unregularized model are optimized to minimize the mean square error over a batch of data, with the squared error given by

$$\mathcal{L} = (s(x_q, t_q) - D(E(P(x_s, t_s), s(x_q, t_q), PE(x_q))))^2. \quad (10)$$

The batch is defined by hyper parameters determining number of frames and number of pixels per frame. The algorithm to minimize the mean squared error is Adam, with learning rate  $1 \times 10^{-4}$ .

### 4.2 Experiments

Beyond the baseline validation on the training data, we conducted two additional experiments to test the Senseiver reconstructions. We perturbed the eight training epicenters to probe the extrapolatory capability of the model. We emphasize that none of the frames of these perturbed epicenter simulations are included in the training set. We refer to this data as the unseen epicenters. These epicenters are depicted visually in relation to the training epicenters in Figure 4. The distances of the unseen epicenters from their closest training epicenter ranges from 2.78 miles to 119.97 miles. To assess the physical consistency of the reconstructions, we train models with a regularization penalty based on the SWE continuity equation (8) and compare the results to the unregularized models.

The error metric we use to evaluate our models is scaled by the absolute max wave height for each frame, and is computed only over pixels achieving a value of at least  $1 \times 10^{-4}$  in the true field. This pixel restriction mitigates the issue of artificially low error due to most of the wave height field over the ocean being identically 0. For each frame we compute the absolute difference between the true and reconstructed wave height fields, and divide by the maximum absolute true wave height for that frame. As a formula, this

is:

$$\text{Error}(x, y, t) = \frac{|\text{True}(x, y, t) - \text{Predicted}(x, y, t)|}{\max(|\text{True}(x, y, t)|)}. \quad (11)$$

In the discussion section, we refer to (Marcato et al., 2023), where a training procedure is implemented that allows the Senseiver to deduce optimal sensor placements. To enhance this discussion, we include the results of an experiment where the training data is augmented with artificial sensors.

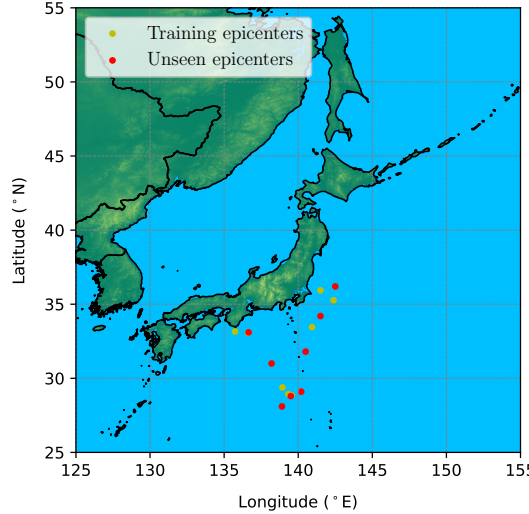


Figure 4: Training (black) and Unseen (red) epicenters used for synthetic tsunami generation.

## 5 Results

### 5.1 Extrapolation to Unseen Data

Evaluating the 0-2 hour model across all epicenters and times of the training set yields an error of  $5.6 \times 10^{-2}$ , whereas the same evaluation for the 2-4 hour model yields an error of  $7.22 \times 10^{-3}$ . This order of magnitude difference in error between the two models derives from the extremely ill-posed reconstruction problem occurring for the early time frames in the 0-2 hour model. The wave height fields at  $t = 0$  consist of a Gaussian supported over a small neighborhood of the epicenter, resulting in null to negligible information to the sensors. This is an encouraging finding, as it would be undesirable for the Senseiver to memorize its training data. In other words, if the problem is ill-posed to the degree of having no meaningful unique solution, we want the reconstruction to have high error, which implies that the model is not overfit and memorizing its data. In the discussion section, we consider strategies to enhance informational content afforded to the model from the perspectives of optimal sensor placement and integration of alternative remote sensing measurements. Across the eight epicenters in the training data, we measured a mean "trigger time" of 30.4 minutes for enough sensor information to generate a reconstruction error no greater than  $1 \times 10^{-1}$ . In contrast, the 2-4 hour models never exceed a reconstruction error of  $2 \times 10^{-2}$ . For the unseen epicenters, the overall error for the 0-2 hour model is  $8.64 \times 10^{-2}$ , with a mean trigger time to achieve a reconstruction error no greater than  $1 \times 10^{-1}$  of 59.5 minutes. For the 2-4 hour model, the overall error is  $2.78 \times 10^{-2}$ .

In Figure 5, we contrast the reconstructions at times 12.5 minutes and 70.8 minutes for epicenter ( $142.5^\circ E, 36.2^\circ N$ ). The closest epicenter in the training set is separated from this epicenter by a distance of 64.8 miles. We note that at 12.5 minutes, only two sensors are visibly near the support of the tsunami wave, which grows to five sensors at 70.8 minutes. These time frames are selected to give an impression of how the reconstruction quality differs before and after the empirical low-quality cut off time (59.5 minutes). Inspecting the reconstruction at 12.5 minutes, we see qualitatively a close estimate of the epicenter location, as well as a close estimate of the support of the first spatial period of the phase. The max amplitude of the reconstruction is  $\approx 80\%$  of the true max amplitude, and the reconstruction fails to capture the two-period nature of the spatial phase in the true field. For the reconstruction at 70.8 minutes, we observe much improved reconstruction accuracy, with remarkable agreement in phase field extent. In the bottom left panel, we plot the error profile as a function of time, showing a steep drop in error during the first  $\approx 60$  minutes of the simulation. Despite the high reconstruction error for early time frames, we observe high accuracy of waveforms recorded at fixed sensor gauges. As evidenced by the wave height time series, we see that the Senseiver is accurately estimating waveforms at the sensor gauges. While it is true that these values are the inputs to the model, there is no bias in the auto encoding process to favor accurate reconstruction at these locations. Rather, the attention mechanism is the likely reason for why we see accurate reconstruction for all times at the sensor locations. We note here that the machine learning based forecasting method proposed in (Liu et al., 2021) was not able to accurately predict wave heights at sensor gauges until 30–60 minutes after the seismic event. Thus, our approach achieves the benchmark goal referenced in (Rim et al., 2022), in addition to providing full-field reconstruction capabilities.

In the 2-4 hour model, we see strong reconstruction accuracy for all times. In this model, no unseen frame ever exceeds an error of .10, so we did not report such a threshold time. In Figure 6, we present a set of representative sample reconstructions for the epicenter at ( $138.9^\circ E, 28.1^\circ N$ ) at times 133.3 minutes, 181.7 minutes, and 225.0 minutes. We note that the closest epicenter from the training set is separated from this epicenter by 63.1 miles. Inspection of the reconstructions show that both the phase field support, number of periods, and amplitude are well approximated by the Senseiver. Inspection of the waveform time series at DART buoys ( $135^\circ E, 29^\circ N$ ) and ( $156^\circ E, 19^\circ N$ ) shows reasonable accuracy to the PDE model, with deviations coming from extra oscillations, slight phase offsets, and slight overestimation of amplitude. Remarkably, this detail is predicted by the Senseiver from only 7, 9, and 11 sensors within the clearly visible support of the phase. Unlike the 0-2 hour model, every frame has suitably informative sensor measurements to yield accurate reconstruction, so there is no noticeable decay in the error profiles for this model.

## 5.2 Physical Consistency

By default, the Senseiver is trained by minimizing the mean squared error between the input frame and the reconstructed frame. For the tsunami data, we added the option to regularize the loss based on the physical consistency of the reconstructions. This physical consistency term is referred to as a soft constraint. The soft constraint in the loss function is based on the conservation of mass equation (2) in the SWE equation pair. A second order approximation to this equation is obtained by balancing the backward finite difference of the wave heights with the average of the divergence of the product of the wave heights and the horizontal divergence

$$\frac{h_n - h_{n-1}}{\Delta t} = -\frac{(\nabla \cdot (hu)_n + \nabla \cdot (hu)_{n-1})}{2}. \quad (12)$$

At each frame of the simulation, the solver can be used to save the  $\nabla \cdot (uh)$  fields along with the wave height. Denoting by  $\hat{h}_n$  the wave height reconstruction at time index  $n$ ,

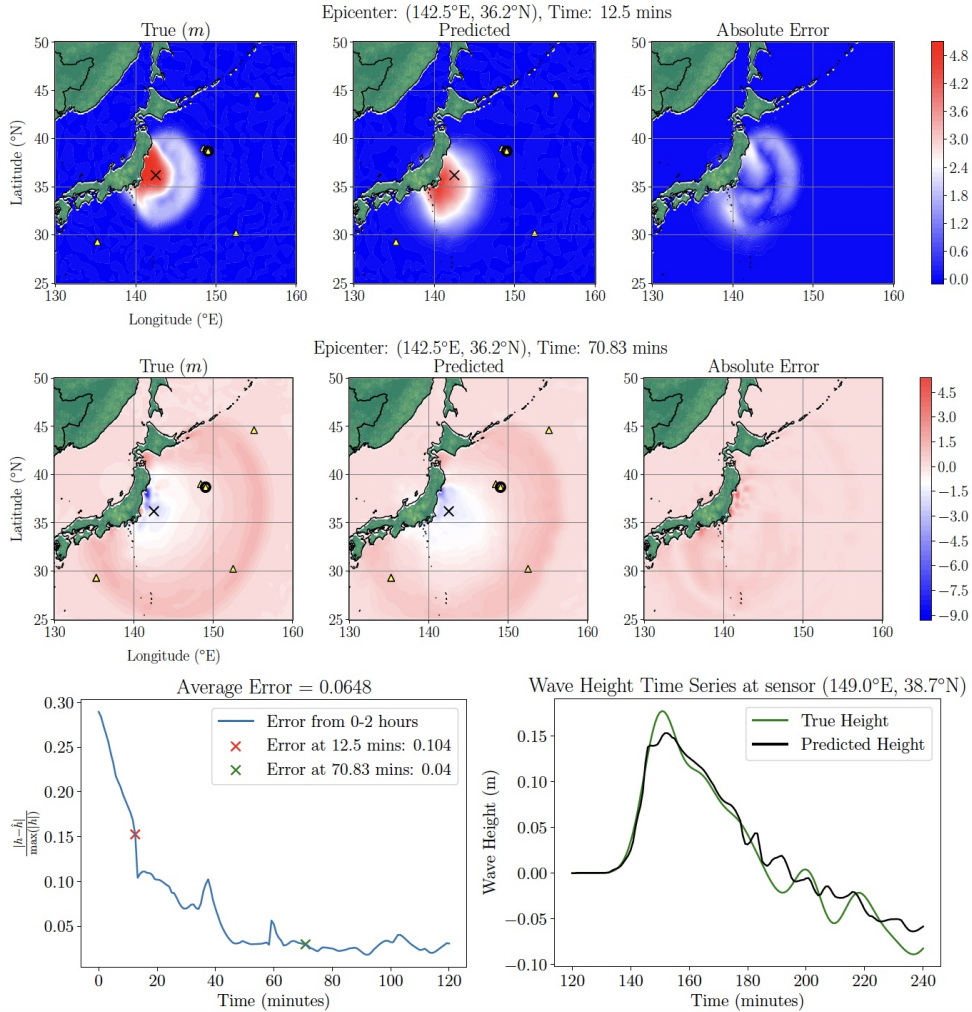


Figure 5: Reconstructions at 12.5 minutes (top rows) and 70.8 minutes (middle row) for epicenter location  $(142.5^\circ E, 36.2^\circ N)$ . The left panel shows the true field, the middle panel shows the predicted field, and the right panel shows the absolute error. The epicenter location is indicated by an X, and yellow triangles notate the sensors. The bottom left panel shows the error profile as a function of time. The error drops below 10% permanently after 37.5 minutes. The red X indicates the time step corresponding to the top row reconstruction, and the green X corresponds to the middle row reconstruction. The bottom right panel shows the waveform at fixed DART buoy with longitude-latitude coordinate  $(149.0^\circ E, 38.7^\circ N)$ . This buoy is distinguished in the reconstructions with a circle.

the modified loss function may then be written:

$$L = MSE(\hat{h}_n, h_n) + \lambda MSE\left(\frac{\hat{h}_n - h_{n-1}}{\Delta t}, -\frac{(\nabla \cdot (hu)_n + \nabla \cdot (hu)_{n-1})}{2}\right)$$

To measure the physical consistency of the reconstructions, we estimate the time derivatives of the wave height using a backward difference, and compare this value to the average of the divergence terms saved in the SWE solver. We trained the model for  $\lambda = 0$  and  $\lambda = 100$ , and found no appreciable gain in physical consistency, nor reconstruction accuracy. For the 0-2 hour model, the mean reconstruction error changed from

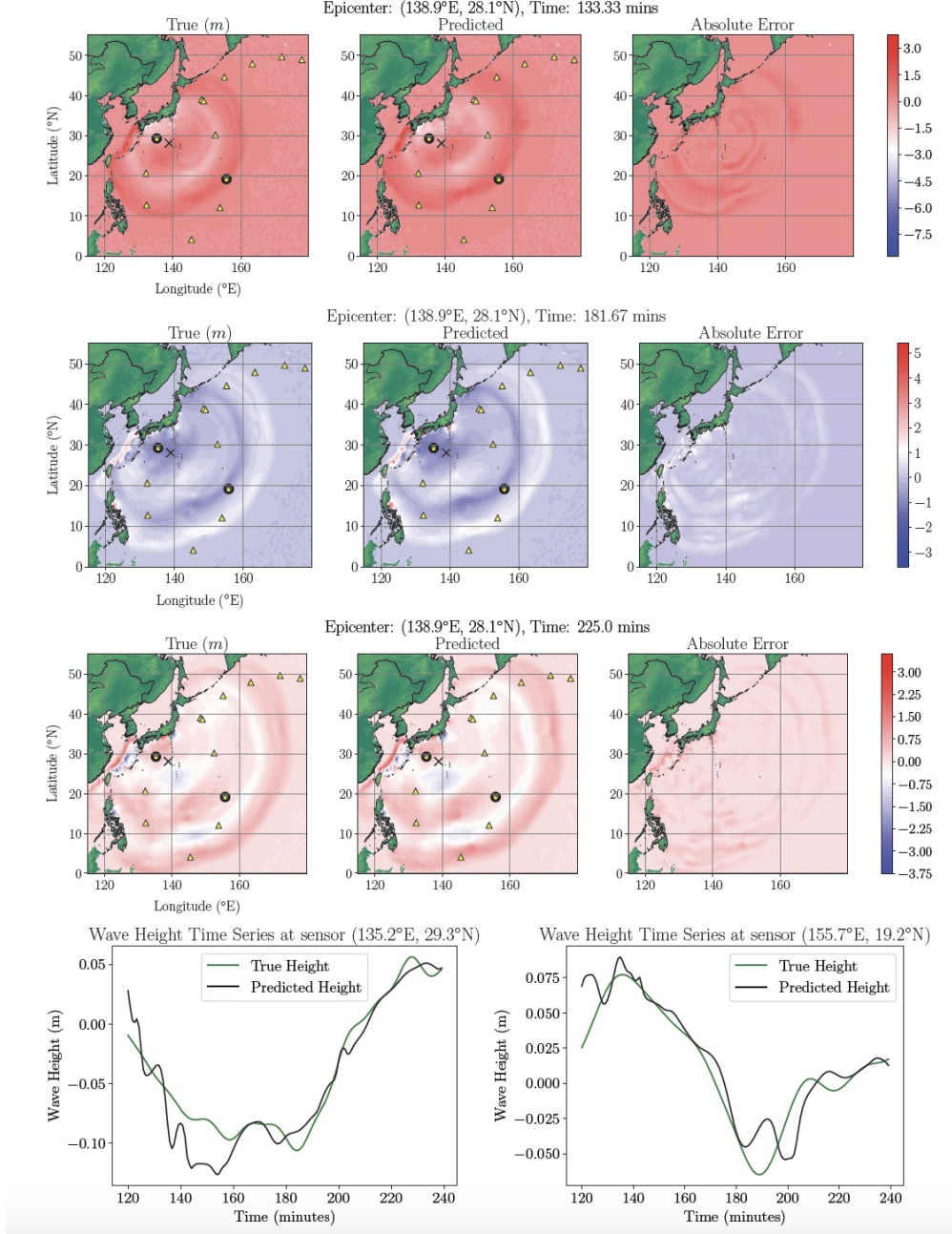


Figure 6: Sample full-field and waveform time series reconstructions on unseen epicenter ( $138.9^{\circ}\text{E}$ ,  $28.1^{\circ}\text{N}$ ) at 133.33 minutes, 181.67 minutes and 225.0 minutes from top to bottom. In the reconstruction plots, the X annotates the epicenter location, the yellow triangles annotate the sensor locations, and the black circles indicate which sensors are used for the time series plots. The time series depict the wave height measured at sensor locations ( $132.5^{\circ}\text{E}$ ,  $29.3^{\circ}\text{N}$ ) and ( $155.7^{\circ}\text{E}$ ,  $19.2^{\circ}\text{N}$ ) from two to four hours after the seismic event.

$8.6 \times 10^{-2}$  to  $8.8 \times 10^{-2}$ , and the consistency error remained the same at  $6.8 \times 10^{-2}$ .

For the 2-4 hour model, the reconstruction error changed from  $2.8 \times 10^{-2}$  to  $2.9 \times 10^{-2}$ , and the consistency error remained the same at  $4.0 \times 10^{-2}$ .

In both cases the continuity equation error from the reconstructions line up closely with the expected numerical error from the SWE solver. In Figure 7, we compare the wave height time derivative of the unregularized model with those of the SWE solver, showing close agreement on large scale features of the phase field. We also show a sample temporal error plot for the continuity equation compared against the corresponding error for the SWE PDE surrogate model, where we have used the unregularized model. We note that the Senseiver error is lower than the SWE error for all times, and that the error profiles have the same shape. These results suggest that the model solves the sparse reconstruction problem in a physically consistent manner, even in the absence of a soft constraint.

## 6 Discussion

Our results demonstrate remarkable full field reconstruction accuracy for unseen epicenters deriving from incredibly sparse measurements, provided sufficiently rich information content has propagated to the sensors. The time lag for information to propagate to the sensors depends on the distance of the epicenter to the observation locations. While the full-field sparse sensing problem is highly ill-posed for early time frames, we find that the recovered wave forms at fixed observation points are accurate for all times. This is in contrast to the forecasting method in (Liu et al., 2021), where inference at observation gauges could not be attempted until 30-60 minutes after the seismic event. As no pixels are favoured during the training process, the accurate wave form recoveries at DART locations are attributed to the attention mechanism used in our method. While our experiments are conducted to assess high-resolution reconstructions, the Senseiver can be used to query any set of pixel locations. Introducing weightings to the queried pixels could be a viable method to generate a pre-specified set of observation points, as is done in (Wang et al., 2019), which could then be used as input to the Green's Function based data assimilation method (Wang, 2022). The above suggestion provides a road map to integrate the Senseiver architecture with existing data assimilation methods, and is saved for future work.

To improve the accuracy of high-resolution full-field reconstructions at early time frames, it is essential that the Senseiver is provided richer information content. The first information enhancement method we consider is that of optimal sensor placement. We briefly list some notable examples of research efforts in this area. In (Magdalena et al., 2021), an optimal configuration of bottom pressure recorders (BPR) is proposed as the solution to a bathymetry constrained particle swarm optimization (PSO) problem, where an SWE solver is used to flag locations achieving a minimal arrival time, and the bathymetry constraint is used to confine admissible locations to cost effective ocean depths. Optimal offshore sensor arrangements are considered in (Meza et al., 2020) and (Lee et al., 2020). In the former, optimal arrangement is probed by optimizing an objective dependent on arrival time, amplitude, and forecast skill, and depends on an inversion algorithm to estimate the tsunami source. In the latter, sensor arrangements are determined by defining a high probability detection region based on 39 numerical experiments. Much more in line with this work, (Fujita et al., 2024) consider optimal placement of in-ocean sensors, using a proper orthogonal decomposition (POD) approach heavily inspired by (Manohar et al., 2018). They initialize a set of  $n$  sensor locations, with the goal of extracting a much smaller set of  $p$  sensor locations that retain sufficient information to deduce full-field waveform characteristics. The method involves using an SWE solver to collect wave height time series at each location, and then concatenates all the time series into a data matrix, from which the optimal locations are derived from a POD procedure. Their goal is to reconstruct a set of  $n$  wave height time series given  $p$  wave height time series, where  $p < n$ . While the above results are promising, all but one considers

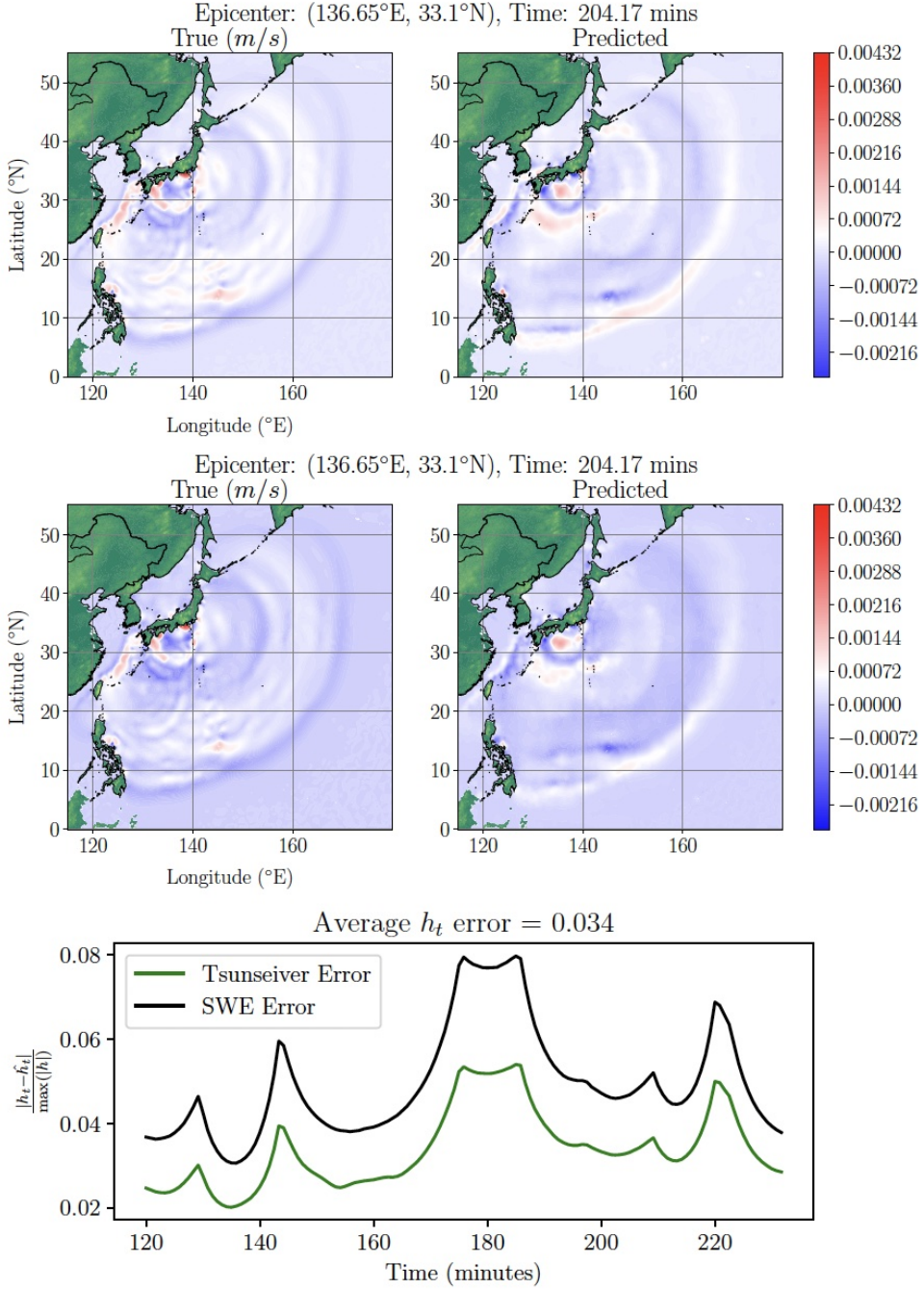


Figure 7: Wave height time derivative reconstruction at 204.2 minutes for unregularized (top) and regularized (middle) model. Temporal continuity equation error from 2-4 hours (bottom) for epicenter ( $136.7^{\circ}E, 33.1^{\circ}N$ ) for unregularized model.

in-ocean sensor arrays, and none of them seek to reconstruct the full-field. In (Marcato et al., 2023), the Senseiver architecture is modified to allow varying sensor locations during training. Specifically, the sensor positions are parameterized in the network such that the sensor positions are trainable, and their final state is taken to be an optimal configuration. Moreover, the sensor exploration during training provides enhanced spatial aware-

ness of the model. For practical purposes, one could use this procedure to recommend  $n$  additional DART buoy deployments, or re-position existing DART buoys. While we did not test the differentiable sensor placement concept in this work, we conduct a simple experiment to demonstrate the beneficial effect of additional information. Applying  $k$ -means clustering to the USGS earthquake dataset (with  $k = 3$ ), we added three artificial sensor locations to the DART array, and trained a model in the 0-2 hour regime. With three additional sensors, the mean error across all epicenters dropped from  $8.6 \times 10^{-2}$  to  $6.1 \times 10^{-2}$ . The mean trigger time to observe no errors exceeding  $1 \times 10^{-1}$  decreased from 59.5 minutes to 43.3 minutes. In Figure 8, we compare a reconstruction with and without the additional sensors.

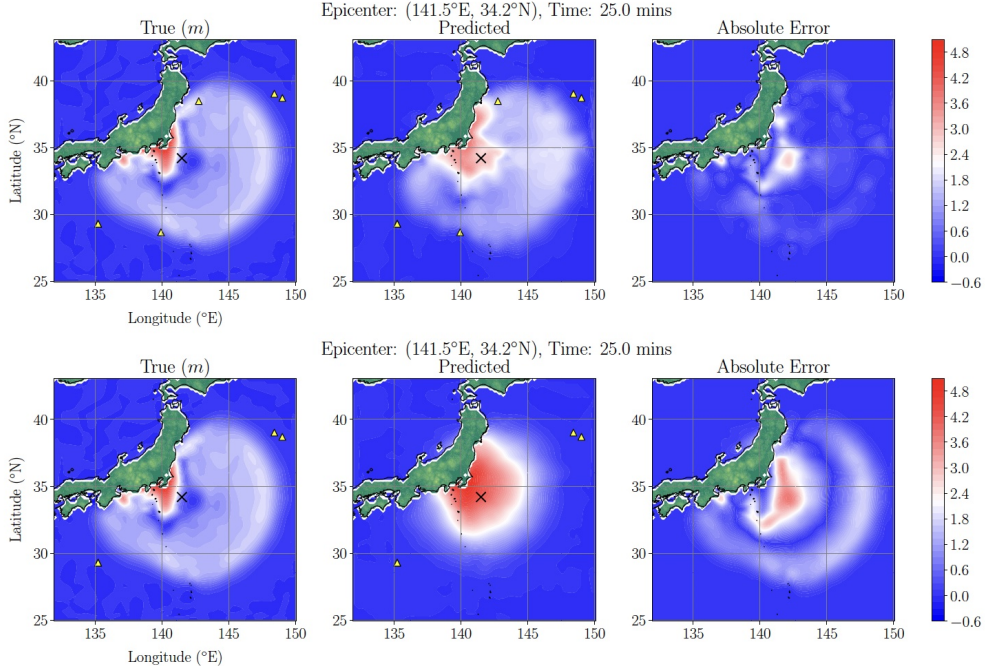


Figure 8: Reconstruction comparison for epicenter ( $141.5^{\circ}E, 34.2^{\circ}N$ ) at 25.0 minutes with (top) and without (bottom) the addition of artificial sensors.

A second avenue of information enhancement is to consider non ocean-source information. This was utilized in (Rim et al., 2022) where satellite information was used to deduce wave form time series within 9 minutes of the seismic event. One of the key strengths of the Senseiver architecture is its flexibility with respect to input structure, and this flexibility can be leveraged to incorporate arbitrary information. In recent years, diverse information sources have been proposed in the machine learning and data assimilation based tsunami forecasting literature. Examples include HF Radar (Wang, Imai, Mulia, et al., 2023), satellite (Mulia et al., 2020),(Mulia et al., 2022), and acoustic sensing (Xiao et al., 2024). In addition, there are other existing ocean-based sensor networks such as S-net which have been used for tsunami prediction (Takahashi & Imai, 2022), (Wang, Imai, Miyashita, et al., 2023). Any combination of these information sources can be incorporated into the Senseiver by way of its positional encoder, or as additional sensor inputs made compatible with existing sensor inputs by way of embeddings and trainable arrays. We save such experiments for future work.

## 7 Conclusions

We have demonstrated that the Senseiver can reconstruct accurate tsunami waves from sparse observations corresponding to real-world DART buoy locations. Given very few sensor input sources, the reconstructions capture both the support and finer features of the phase, as well as the maximum amplitude. We tested the Senseiver on epicenters not seen in training, where the epicenter distance from the training set varied from 2.8 miles to 120.0 miles. These tests showed good extrapolatory capabilities, and indicated a relationship between reconstruction quality and epicenter proximity to the training set. We also tested the physical consistency of the model, finding that its continuity equation error aligns closely with the error exhibited by the PDE simulation, even in the absence of regularization. Notably, these experiments mark the first time a Senseiver-based model has been trained on a dataset with mixed initial conditions, as well as the first time such a model has been used for inference on initial conditions outside of the training set. We suggested that the model as is could be used to generate dense observations for the Green's Function based data assimilation forecasting method.

We encountered in our experiments sensor input configurations that lack sufficient information to yield accurate reconstructions. As expected, these occur at and just after the onset of a tsunami. While there are tsunami scenarios for which the time between informative sensor readings and inundation is long enough to make the Senseiver useful as is, we discussed methods to resolve information-theoretic limits imposed by our restriction to the DART buoys. Firstly, we suggested a differentiable sensor placement procedure (Marcato et al., 2023) that can be performed to find optimal sensor positions for existing and/or new DART buoys, and accompanied this discussion with a demonstration of reconstruction improvements given three additional sensors. Secondly, we discussed a wide range of data sources used in the machine learning and data assimilation literature, and suggested that the ability to encode arbitrary coordinates into the Senseiver greatly increases the information content it can utilize. Future work should focus on using the Senseiver to test and deduce optimal sensor placements, as well as develop ways to incorporate additional sensor sources into the positional encoder.

## 8 Open Research

The code and data for this project will be uploaded to github after publication.

### Acknowledgments

This project was partially funded by the Artimis LDRD program at the Los Alamos National Laboratory

### References

Archambault, T., Filoche, A., Charantonis, A., Béréziat, D., & Thiria, S. (2024). Learning sea surface height interpolation from multi-variate simulated satellite observations. *Journal of Advances in Modeling Earth Systems*, 16(6), e2023MS004047. Retrieved from <https://agupubs.onlinelibrary.wiley.com/doi/abs/10.1029/2023MS004047> (e2023MS004047 2023MS004047) doi: <https://doi.org/10.1029/2023MS004047>

Barton, K. N., Pal, N., Brus, S. R., Petersen, M. R., Arbic, B. K., Engwirda, D., ... Schindelegger, M. (2022). Global barotropic tide modeling using inline self-attraction and loading in MPAS-Ocean. *Journal of Advances in Modeling Earth Systems*, 14(11), e2022MS003207.

Berger, M. J., George, D. L., LeVeque, R. J., & Mandli, K. T. (2011). The GeoClaw software for depth-averaged flows with adaptive refinement. *Advances in Water Resources*, 34(9), 1195–1206.

Bernard, E., & Titov, V. (2015, 10). Evolution of tsunami warning systems and products. *Philosophical transactions. Series A, Mathematical, physical, and engineering sciences*, 373. doi: 10.1098/rsta.2014.0371

Engwirda, D. (2017). JIGSAW-GEO: locally orthogonal staggered unstructured grid generation for general circulation modelling on the sphere. *Geoscientific Model Development*, 10(6), 2117–2140.

Fujii, Y., Satake, K., Sakai, S., Shinohara, M., & Kanazawa, T. (2011). Tsunami source of the 2011 off the Pacific coast of Tohoku Earthquake. *Earth, planets and space*, 63(7), 815–820.

Fujita, S., Nomura, R., Moriguchi, S., Otake, Y., Koshimura, S., Leveque, R., & Terada, K. (2024, 02). Optimization of a tsunami gauge configuration for pseudo-super-resolution of wave height distribution. *Earth and Space Science*, 11. doi: 10.1029/2023EA003144

GEBCO Compilation Group. (2023). *GEBCO 2023 Grid*. (doi:10.5285/f98b053b-0cbc-6c23-e053-6c86abc0af7b)

Imamura, F., Boret, S., Suppasri, A., & Muhari, A. (2019, 05). Recent occurrences of serious tsunami damage and the future challenges of tsunami disaster risk reduction. *Progress in Disaster Science*, 1, 100009. doi: 10.1016/j.pdisas.2019.100009

Inazu, D., & Saito, T. (2013). Simulation of distant tsunami propagation with a radial loading deformation effect. *Earth, Planets and Space*, 65, 835–842.

Lee, E., Jung, T., & Shin, S. (2020, 09). Numerical and probabilistic study on the optimal region for tsunami detection instrument deployment in the eastern sea of korea. *Applied Sciences*, 10, 6071. doi: 10.3390/app10176071

LeVeque, R. J., George, D. L., & Berger, M. J. (2011). Tsunami modelling with adaptively refined finite volume methods. *Acta Numerica*, 20, 211–289.

Lilly, J. R., Capodaglio, G., Petersen, M. R., Brus, S. R., Engwirda, D., & Higdon, R. L. (2023). Storm surge modeling as an application of local time-stepping in MPAS-Ocean. *Journal of Advances in Modeling Earth Systems*, 15(1), e2022MS003327.

Lilly, J. R., Engwirda, D., Capodaglio, G., Higdon, R. L., & Petersen, M. R. (2023). CFL Optimized Forward–Backward Runge–Kutta Schemes for the Shallow-Water Equations. *Monthly Weather Review*, 151(12), 3191–3208.

Liu, C., Rim, D., Baraldi, R., & Leveque, R. (2021, 12). Comparison of machine learning approaches for tsunami forecasting from sparse observations. *Pure and Applied Geophysics*, 178. doi: 10.1007/s00024-021-02841-9

Maeda, T., Obara, K., Shinohara, M., Kanazawa, T., & Uehira, K. (2015, 10). Successive estimation of a tsunami wavefield without earthquake source data: A data assimilation approach toward real-time tsunami forecasting. *Geophysical Research Letters*, 42. doi: 10.1002/2015GL065588

Magdalena, I., La'lang, R., Mendoza, R. G., & Lope, J. E. C. (2021). Optimal placement of tsunami sensors with depth constraint. *PeerJ Computer Science*, 7. Retrieved from <https://api.semanticscholar.org/CorpusID:240071378>

Manohar, K., Brunton, B., Kutz, J., & Brunton, S. (2018, 05). Data-driven sparse sensor placement for reconstruction. *IEEE control systems*, 38, 63-. doi: 10.1109/MCS.2018.2810460

Marcato, A., O'Malley, D., Viswanathan, H., Guiltinan, E., & Santos, J. E. (2023). *Reconstruction of fields from sparse sensing: Differentiable sensor placement enhances generalization*.

Meza, J., Catalán, P., & Tsushima, H. (2020, 03). A multiple-parameter methodology for placement of tsunami sensor networks. *Pure and Applied Geophysics*, 177. doi: 10.1007/s00024-019-02381-3

Mulia, I., Hirobe, T., Inazu, D., Endoh, T., Niwa, Y., Gusman, A., ... Hibiya, T. (2020, 02). Advanced tsunami detection and forecasting by radar on unconventional airborne observing platforms. *Scientific Reports*, 10. doi:

10.1038/s41598-020-59239-1

Mulia, I., Ueda, N., Miyoshi, T., Gusman, A., & Satake, K. (2022, 09). Machine learning-based tsunami inundation prediction derived from offshore observations. *Nature Communications*, *13*, 5489. doi: 10.1038/s41467-022-33253-5

NOAA. (2011). *National Data Buoy Center – DART*. (<http://www.ndbc.noaa.gov/dart.shtml>)

Pal, N., Barton, K. N., Petersen, M. R., Brus, S. R., Engwirda, D., Arbic, B. K., ... Wirasaet, D. (2023). Barotropic tides in MPAS-Ocean (E3SM V2): impact of ice shelf cavities. *Geoscientific Model Development*, *16*(4), 1297–1314.

Popinet, S. (2012). Adaptive modelling of long-distance wave propagation and fine-scale flooding during the Tohoku tsunami. *Natural Hazards and Earth System Sciences*, *12*(4), 1213–1227.

Popinet, S. (2020). A vertically-Lagrangian, non-hydrostatic, multilayer model for multiscale free-surface flows. *Journal of Computational Physics*, *418*, 109609.

Rim, D., Baraldi, R., Liu, C. M., LeVeque, R. J., & Terada, K. (2022). Tsunami early warning from global navigation satellite system data using convolutional neural networks. *Geophysical Research Letters*, *49*(20), e2022GL099511.

Ringler, T., Thuburn, J., Klemp, J., & Skamarock, W. (2010). A unified approach to energy conservation and potential vorticity dynamics for arbitrarily-structured C-grids. *Journal of Computational Physics*, *229*(9), 3065–3090.

Santos, J. E., Fox, Z. R., Mohan, A., O’Malley, D., Viswanathan, H., & Lubbers, N. (2023). Development of the Senseiver for efficient field reconstruction from sparse observations. *Nature Machine Intelligence*, 1–9.

Takahashi, N., & Imai, K. (2022, 02). Realtime tsunami prediction system using ocean floor network for local regions. *Applied Sciences*, *12*, 1627. doi: 10.3390/app12031627

Thuburn, J., Ringler, T., Skamarock, W., & Klemp, J. (2009). Numerical representation of geostrophic modes on arbitrarily structured C-grids. *Journal of Computational Physics*, *228*(22), 8321 - 8335.

Titov, V. V., & Gonzalez, F. I. (1997). Implementation and testing of the method of splitting tsunami (MOST) model.

Wang, Y. (2022, 10). Green’s function-based tsunami data assimilation (gftda). In (p. 19-43). doi: 10.1007/978-981-19-7339-0\_2

Wang, Y., Imai, K., Miyashita, T., Ariyoshi, K., Takahashi, N., & Satake, K. (2023, 10). Coastal tsunami prediction in tohoku region, japan, based on s-net observations using artificial neural network. *Earth Planets and Space*, *75*, 154. doi: 10.1186/s40623-023-01912-6

Wang, Y., Imai, K., Mulia, I. E., Ariyoshi, K., Takahashi, N., Sasaki, K., ... Sato, Y. (2023). Data Assimilation Using High-Frequency Radar for Tsunami Early Warning: A Case Study of the 2022 Tonga Volcanic Tsunami. *Journal of Geophysical Research: Solid Earth*, *128*(2), e2022JB025153.

Wang, Y., Maeda, T., Satake, K., Heidarzadeh, M., Su, H.-Y., Sheehan, A., & Gusman, A. (2019, 02). Tsunami data assimilation without a dense observation network. *Geophysical Research Letters*, *46*. doi: 10.1029/2018GL080930

Xiao, H., Spica, Z., Li, J., & Zhan, Z. (2024, 01). Detection of earthquake infragravity and tsunami waves with underwater distributed acoustic sensing. *Geophysical Research Letters*, *51*. doi: 10.1029/2023GL106767

## Appendix A Training Epicenters

	Simulation Coordinates							
Coordinate	Epi 1	Epi 2	Epi 3	Epi 4	Epi 5	Epi 6	Epi 7	Epi 8
Longitude	136.62	139.56	139.33	138.94	140.93	135.74	141.50	142.39
Latitude	33.07	28.86	28.93	29.38	33.45	33.16	35.94	35.27

## Appendix B Unseen Epicenters

	Simulation Coordinates							
Coordinate	Epi 1	Epi 2	Epi 3	Epi 4	Epi 5	Epi 6	Epi 7	Epi 8
Longitude	136.65	138.20	138.90	139.50	140.20	140.50	141.50	142.50
Latitude	33.10	31.00	28.10	28.80	29.10	31.80	34.20	36.20